# Search with UVES and XSHOOTER for signatures of the low-mass secondary in the post common-envelope binary AA Dor \*, \*\*, \*\*\*

D. Hoyer<sup>1</sup>, T. Rauch<sup>1</sup>, K. Werner<sup>1</sup>, P. H. Hauschildt<sup>2</sup>, and J. W. Kruk<sup>3</sup>

- Institute for Astronomy and Astrophysics, Kepler Center for Astro and Particle Physics, Eberhard Karls University, Sand 1, 72076 Tübingen, Germany
  - e-mail: rauch@astro.uni-tuebingen.de
- Hamburger Sternwarte, Gojenbergsweg 112, 21029 Hamburg, Germany
- NASA Goddard Space Flight Center, Greenbelt, MD 20771, USA

#### **ABSTRACT**

Context. AA Dor is a close, totally eclipsing, post common-envelope binary with an sdOB-type primary star and an extremely lowmass secondary star, located close to the mass limit of stable central hydrogen burning. Within error limits, it may either be a brown

Aims. We aim to extract the secondary's contribution to the phase-dependent composite spectra. The spectrum and identified lines of

Methods. In January 2014, we measured the phase-dependent spectrum of AA Dor with XSHOOTER over one complete orbital period. Since the secondary's rotation is presumable synchronized with the orbital period, its surface strictly divides into a day and night side. Therefore, we may obtain the spectrum of its cool side during its transit and of its hot, irradiated side close to its occultation. We developed the Virtual Observatory (VO) tool TLISA to search for weak lines of a faint companion in a binary system.

Results. We identified 53 spectral lines of the secondary in the ultraviolet-blue, visual, and near-infrared XSHOOTER spectra that are strongest close to its occultation. We identified 57 (20 additional) lines in available UVES (Ultraviolet and Visual Echelle Spectrograph) spectra from 2001. The lines are mostly from C II - III and O II, typical for a low-mass star that is irradiated and heated by the primary. We verified the orbital period of  $P = 22597.033201 \pm 0.00007$  s and determined the orbital velocity  $K_{\text{sec}} = 232.9^{+16.6}_{-6.5}$  km/s of the secondary. The mass of the secondary is  $M_{\text{sec}} = 0.081^{+0.018}_{-0.010} M_{\odot}$  and, hence, it is not possible to reliably determine a brown

Conclusions. Although we identified many emission lines of the secondary's irradiated surface, the resolution and signal-to-noise ratio of our UVES and XSHOOTER spectra are not good enough to extract a good spectrum of the secondary's nonirradiated hemi-

Key words. Stars: abundances – Stars: binaries: eclipsing – Stars: low-mass – Stars: individual: AA Dor – Stars: individual: LB 3459

Tübingen, Germany
e-mail: rauch@astro.uni-tuebingen.de

2 Hamburger Sternwarte, Gojenbergsweg 112, 21029 Hamburg, G
3 NASA Goddard Space Flight Center, Greenbelt, MD 20771, US

Received 31 March 2015; accepted 25 April 2015

ABST

Context. AA Dor is a close, totally eclipsing, post common-envelor mass secondary star, located close to the mass limit of stable centrol dwarf or a late M-type dwarf.

Aims. We aim to extract the secondary's contribution to the phase-the secondary decide on its nature.

Methods. In January 2014, we measured the phase-dependent speriod. Since the secondary's rotation is presumable synchroniz and night side. Therefore, we may obtain the spectrum of its cool occultation. We developed the Virtual Observatory (VO) tool TLIS We successfully applied it to the observations of AA Dor.

Results. We identified 53 spectral lines of the secondary in the that are strongest close to its occultation. We identified 57 (20 accepted Spectrograph) spectra from 2001. The lines are mostly from Ciri-m the primary. We verified the orbital period of P = 22597.033201±0 of the secondary. The mass of the secondary is Msec = 0.081\_-0.01 dwarf or an M-type dwarf nature.

Conclusions. Although we identified many emission lines of the ratio of our UVES and XSHOOTER spectra are not good enough sphere.

Key words. Stars: abundances – Stars: binaries: eclipsing – Starting – virtual observatory tools

1. Introduction

AA Dor (CPD-69°389, HD 269696, LB 3459) was discovered to be a close, short-period, totally eclipsing binary (Kilkenny et al. 1978) with an inclination of i = 89°21 ± 0°30

(Kilkenny et al. 1978) with an inclination of i = 89°21 ± 0°30

(Kilkenny et al. 1978) with an inclination of i = 80°21 ± 0°30

(Kilkenny et al. 1978) with an inclination of i = 80°21 ± 0°30

(Kilkenny et al. 1978) with an inclination of i = 80°21 ± 0°30

(Korheiber & Gänsicke 2003) with a sdOB-type primary star and a low-mass companion (Rauch 2004). Its orbital period P = 0.261 539 7363(4)d (constant at a level of about 10<sup>-14</sup> d per and a low-mass companion (Rauch 2004). Its orbital period P = 0.2615397363(4) d (constant at a level of about  $10^{-14} d$  per orbit) was determined by Kilkenny (2011) with high accuracy from the light curve, using eclipses from 1977 to 2010.

AA Dor belongs to the class of HW Vir-type variables. These are eclipsing binaries consisting of a B-type subdwarf star and a late M-type star. They experienced a common-envelope phase when the primary star evolved through a red-giant phase. Their orbital periods are generally short ( $P \approx 0.1$  d, Heber 2009). They are of great importance because eclipsing binaries allow precise mass determinations. Presently, we know more than 15 of these systems (Ritter & Kolb 2003; Almeida et al. 2012; Barlow et al. 2013; Schaffenroth et al. 2013, 2014, 2015). Yet another sdOBtype member was discovered (NSVS 14256825, Almeida et al. 2012). AA Dor is of special importance because it is one of the hottest members with one of the longest periods. It is one of the brightest ( $m_V = 11.138$ ) and, hence, best-studied HW Vir-type binaries.

AA Dor is a precataclysmic variable (Ritter 1986) and, thus, stringent constraints for the mass of the low-mass secondary, just at the limit of the hydrogen-burning mass, and its angular momentum are a prerequisite for reliable common-envelope modeling, especially the ejection mechanism (Livio & Soker 1984) and predictions of the evolution of AA Dor. Therefore, it is a key object for understanding common-envelope evolution.

Several spectral analyses by means of nonlocal thermodynamic equilibrium (NLTE) model atmospheres were performed, and the primary star of AA Dor (LB 3459) turned out to be one of

<sup>\*</sup> Based on observations collected at the European Southern Observatory, Chile, programs 066.D-1800 and 092.C-0692.

<sup>\*\*</sup> Based on observations made with the NASA-CNES-CSA Far Ultraviolet Spectroscopic Explorer.

<sup>\*\*\*</sup> Figures 2 - 5, 9, and ?? - ??, are only available in electronic form via http://www.edpsciences.org.

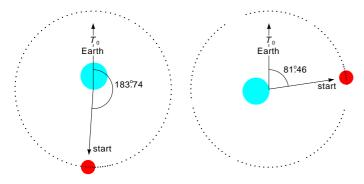


**Fig. 1.** Orbital location of the primary (light blue in the online version) and secondary (red) at the UVES (left) and XSHOOTER (right) observation times. The start times of the two observation campaigns are indicated (HJD 2451917.5191833 and 2456665.5858551, respectively). The stars move counterclockwise. Dots mark the locations of the secondary at the start times of the individual observations.

the hottest sdOB stars ( $T_{\rm eff}$  = 42000 K, Rauch 2000; Fleig et al. 2008). These analyses showed a discrepancy in the surface gravity that was derived by radial-velocity and light-curve analyses (Hilditch et al. 2003),  $\log(g/\text{cm/s}^2) = 5.30 \pm 0.1$  and  $\log g = 5.53 \pm 0.03$ , respectively.

Since Vučković et al. (2008) for the first time identified spectral lines of the secondary in spectra obtained with the Ultraviolet and Visual Echelle Spectrograph (UVES¹) at the European Southern Observatory (ESO) and determined a lower limit ( $K_{\rm sec} \geq 230\pm10~{\rm km/s}$ ) of its radial velocity amplitude, both components' masses are known ( $M_{\rm pri}=0.45~M_{\odot}$ ,  $M_{\rm sec}=0.076~M_{\odot}$ ), however, with rather large error bars. Müller et al. (2010) considered that, because of the refection effect, this measured  $K_{\rm sec}$  comes from the outer edge of the stellar disk. They applied the stellar radius from Rauch (2000,  $R_{\rm sec}=0.135~R_{\odot}$ ) to shift the determined emission radius to the stellar center and used  $K_{\rm sec}=240\pm20~{\rm km/s}$  to calculate the stellar masses. With  $K_{\rm pri}=40.15\pm0.11~{\rm km/s}$ , they derived  $M_{\rm pri}=0.51^{+0.125}_{-0.108}~M_{\odot}$  and  $M_{\rm sec}=0.085^{+0.031}_{-0.023}~M_{\odot}$ .

We recently performed an NLTE spectral analysis of the primary (Klepp & Rauch 2011), where we used a lower rotational velocity of  $v_{\rm rot}=30\,{\rm km/s}$  (Müller et al. 2010; Geier et al. 2010) than before (35 km/s, Fleig et al. 2008). With improved model atmospheres and improved Stark line-broadening tables for H I lines (Tremblay & Bergeron 2009), we determined  $T_{\rm eff}=42000\pm1000\,{\rm K}$  and  $\log g=5.46\pm0.05$ . Thus, the gravity problem is solved. From our mass determination of  $M_{\rm pri}=0.4714\pm0.0050\,M_{\odot}$ , in comparison with evolutionary tracks of postextended horizontal branch (post-EHB) stars (Dorman et al. 1993), we calculated ( $M_{\rm pri}K_{\rm pri}=M_{\rm sec}K_{\rm sec}$ ) the secondary's mass to be  $M_{\rm sec}=0.0725-0.0863\,M_{\odot}$ . Since the hydrogenburning mass limit is about  $0.075\,M_{\odot}$  (Chabrier & Baraffe 1997; Chabrier et al. 2000), the secondary may be either a brown dwarf or a late M-type dwarf.

To make progress in our understanding of common-envelope evolution in general and to further constrain the secondary's nature, we measure the secondary's contribution to the composite spectrum of AA Dor, especially in the infrared and follow its spectral evolution during one complete orbital period. We therefore performed phase-dependent spectroscopy with XSHOOTER<sup>2</sup> (Vernet et al. 2011) since this contribution is of the order of a few percent (Fleig et al. 2008) and, thus, a very

high signal-to-noise ratio (S/N) of the observed spectra is required for its detection.

In Sect. 2, we briefly describe our new XSHOOTER observations and the UVES data used by Rauch & Werner (2003). We determine the orbital period in Sect. 3. We then revisit the sdOB primary (Sect. 4) and demonstrate how the recently determined surface gravity of Klepp & Rauch (2011) impacts the element abundance determination of Fleig et al. (2008). In Sect. 5, we turn to the secondary star of AA Dor and introduce the newly developed, registered Virtual Observatory (VO) tool Tübingen Line Identification and Spectrum Analyzer (TLISA), which is part of the Tübingen German Astrophysical Virtual Observatory (GAVO³) project. Its application to the XSHOOTER and UVES spectra of AA Dor is described. In Sect. 6, we present our results for the orbit dimensions of AA Dor, as well as the masses and radii of its components. We summarize and conclude in Sect. 7.

#### 2. Observations

We took 105 UVES spectra (individual exposure times 180 s, 3743 Å – 4986 Å), which cover a complete orbital period ( $P = 0.26 \,\mathrm{d}$ ), on Jan 8, 2001 (program 066.D-1800) at the Very Large Telescope / Unit Telescope 2 (VLT/UT2, Kueyen). The spectra were subject to the standard reduction provided by ESO. With a slit width of 1"0 projected at the sky, a resolving power  $R \approx 48000$  was achieved. The S/N of the single spectra is about 20 – 30. See Rauch & Werner (2003) for details.

We obtained 300 XSHOOTER spectra (in its three arms,  $UVB^4$ ,  $VIS^5$ , and  $NIR^6$ , each with 100 exposures of 160 s, 170 s, and 34 s, respectively) exactly 13 years later on Jan 8, 2014 (program 092.C-0692) at the VLT/UT3 (Melipal). The observations of AA Dor started at 02:03 UT (air mass 1.4) and ended at 08:31 UT (air mass 2.3), just before morning twilight. The seeing was around 1" for much of the night but deteriorated greatly during the last two observation blocks (OBs), reaching almost 3" for the final OB (Roger Wesson, priv. comm.). We reduced this data with ESO's Reflex Environment (version 2.6, downloaded Feb 13, 2015, XSHOOTER pipeline identifier 2.5.2). The S/N of the spectra is about 30-50.

Figure 1 displays the binary phases at the start times of the individual UVES and XSHOOTER observations. Figures 2-5 show each individual spectrum of the UVES and XSHOOTER observation campaigns. The XSHOOTER spectra are compared with our best model for the primary (see Sect. 4). The synthetic spectrum is normalized to match the 2MASS  $K_s = 12.046$  brightness. A reddening with  $E_{B-V} = 0.08$  is applied following the law of Fitzpatrick (1999, with  $R_V = 3.1$ ). The synthetic spectrum is convolved with a Gaussian to match the XSHOOTER resolution.

# 3. Orbital period

Rauch & Werner (2003) determined an orbital period of  $P = 0.261\,582\,199(58)\,\mathrm{d}$  from the He II  $\lambda\,4686\,\mathrm{\mathring{A}}$  radial-velocity curve. This deviates ( $\approx +0.016\,\%$ ) from that of Kilkenny (2011,  $P = 0.261\,539\,7363(4)\,\mathrm{d}$ ) measured from the light curve. Our XSHOOTER data extended the timebase of the radial-velocity

http://www.g-vo.org

<sup>&</sup>lt;sup>4</sup> ultraviolet-blue, 3000 Å - 5595 Å, R = 4350

<sup>&</sup>lt;sup>5</sup> visual, 5595 Å - 10240 Å, R = 7450

 $<sup>^{6}</sup>$  near infrared, 10240 Å – 24800 Å, R = 5300

http://www.eso.org/sci/facilities/paranal/instruments/uveksthptm//www.ls.eso.org/lasilla/dimm/Archive

http://www.eso.org/sci/facilities/paranal/instruments/x8hbotqesr.h/wmdw.eso.org/sci/software/reflex

curve from 2535 days to 7283 days (including the measurements of Hilditch et al. 1996; Rauch & Werner 2003, and of FUSE observations in 2003 and 2004). We employed the Interactive Data Language (IDL<sup>9</sup>) to measure the Doppler shifts of He II  $\lambda$  4686 Å in the optical and determined those of C III, O vI, Si IV, and P v lines in the far-ultraviolet (FUSE).

We used the TRIPP software package (Schuh et al. 2003; Geckeler et al. 2014) to determine the period (with  $T_0$  = 2451917.15269, the time of mid-transit, Rauch & Werner 2003). We confirmed Kilkenny's light-curve solution (Fig. 6, P = 22597.03320768  $\pm$  0.0000691 s, Sect. 1).

We note that Fig. 4 of Rauch & Werner (2003) is incorrect. In its top panel, the data of Hilditch et al. (1996) is erroneously shown with an offset of +0.5 d, and the  $v_{\rm rad}$  values in the bottom panel have an incorrect sign. This explains the period deviation that was previously found (Sect. 1).

# 4. The primary

To disentangle the composite AA Dor spectra and to extract the secondary's spectrum, we must subtract the primary's contribution, considering its orbital motion, from all spectra. Therefore, we shifted all spectra to rest wavelengths, i.e., we applied a phase-dependent radial-velocity correction for the primary. Then, we coadded the spectra with the best S/N ratio to achieve a master spectrum. The expected weak lines of the secondary smear out in this procedure and leave no detectable marks.

Since the primary's master spectra (separately for UVES and XSHOOTER) allowed us to verify the result of Klepp & Rauch (2011) for the surface gravity ( $\log g = 5.46 \pm 0.05$ ), we decided to calculate a new grid of NLTE atmosphere models with our Tübingen NLTE Model-Atmosphere Package (TMAP<sup>10</sup>; Werner et al. 2003; Rauch & Deetjen 2003; Werner et al. 2012a) to investigate the impact of the higher  $\log q$  on the photospheric abundances that were determined by Fleig et al. (2008), who used  $\log q = 5.3$ . An indication that these abundances may be slightly different is the prominent Balmer-line problem (Napiwotzki & Rauch 1994; Rauch 2000, 2012) due to the underestimation of metal opacities (Bergeron et al. 1993; Werner 1996). The effect is apparently stronger at the higher  $\log g$ (Klepp & Rauch 2011, their Fig. 5). Therefore the abundance determination was repeated. The H, He, C, N, O, Mg, Si, P, S, Fe, and Ni abundances were determined by spectral fits to ultraviolet observations obtained with the International Ultraviolet Explorer (IUE, cf. Rauch 2000) and the Far Ultraviolet Spectroscopic Explorer (FUSE, cf. Fleig et al. 2008) and to our UVES and XSHOOTER spectra. Table 1 shows the adjusted abundance values. The errors are typically  $\pm 0.2$  dex. Significant deviations were found for Mg, Si, P, and Ni. They are not due to the higher  $\log g$  but to an improved spectral fitting.

The Balmer-line problem, however, is still present at the same strength with the new, fine-tuned abundances. An additional model-atmosphere calculation with artificially increased (to 700 times solar, Scott et al. 2015a,b) iron-group (here Ca – Ni) abundances shows that the Balmer-line problem almost vanishes (Fig. 7). This corroborates the suggestion that missing metal opacities and, hence, cooling of the outer atmosphere are in general responsible for the Balmer-line problem. The real opacity source in AA Dor, however, is not known yet. On the one hand, the rotation of its primary ( $v_{\rm rot} = 30 \, {\rm km/s}$ , cf.

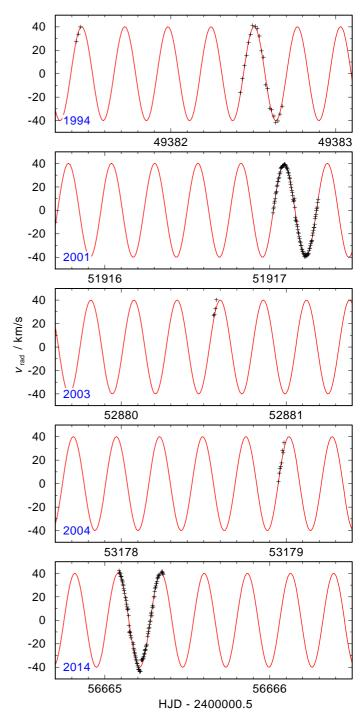


**Fig. 6.** Comparison of radial-velocity measurements of AA Dor with a sine curve calculated with the period of  $P=0.261\,539\,7363\,\mathrm{d}$  from the light-curve solution of Kilkenny (2011).  $K_{\mathrm{pri}}=40.15\,\mathrm{km/s}$  and  $T_0=51917.15269$  are from Müller et al. (2010) and Rauch & Werner (2003), respectively. From top to bottom, the panels show data from Hilditch et al. (1996), Rauch & Werner (2003, UVES), FUSE 2003, FUSE 2004, and our XSHOOTER spectra. The measurements cover the time from Jan 29, 1994, to Jan 8, 2014.

Klepp & Rauch 2011) prohibits the detection of weak metal lines, and on the other hand, trans-iron-group elements (e.g., Werner et al. 2012b; Rauch et al. 2012, 2014a,b, 2015) have been totally neglected so far.

<sup>9</sup> http://www.exelisvis.com/ProductsServices/IDL

<sup>10</sup> http://astro.uni-tuebingen.de/~TMAP

**Table 1.** Photospheric abundances (mass fractions) of the primary of AA Dor, determined by Fleig et al. (2008,  $T_{\rm eff}$  = 42000 K,  $\log g$  = 5.30, denoted F) and in this work (H,  $T_{\rm eff}$  = 42000 K,  $\log g$  = 5.46). Column 4 shows the deviations.

Element	F	Н	(H/F)-1/%
Н	$9.9 \times 10^{-1}$	$9.9 \times 10^{-1}$	0
He	$3.2 \times 10^{-3}$	$2.7 \times 10^{-3}$	-15
C	$1.8 \times 10^{-5}$	$2.0 \times 10^{-5}$	10
N	$4.1 \times 10^{-5}$	$4.6 \times 10^{-5}$	10
O	$1.0 \times 10^{-3}$	$1.1 \times 10^{-3}$	10
Mg	$3.6 \times 10^{-3}$	$4.1 \times 10^{-4}$	-90
Si	$9.7 \times 10^{-5}$	$2.1 \times 10^{-4}$	110
P	$5.2 \times 10^{-6}$	$2.6 \times 10^{-6}$	-50
S	$3.2 \times 10^{-6}$	$3.2 \times 10^{-4}$	100
Fe	$1.2 \times 10^{-3}$	$1.2 \times 10^{-3}$	0
Ni	$3.5 \times 10^{-4}$	$5.2 \times 10^{-4}$	50

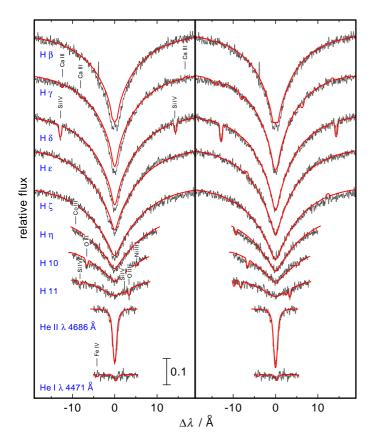


**Fig. 7.** Comparison of synthetic profiles of H and He lines calculated from our models ( $T_{\rm eff}$  = 42000 K, log g = 5.46) with our UVES observation (for clarity smoothed with a low-pass filter, Savitzky & Golay 1964). Left panel: abundances from Table 1, and Sc, Ti, V, Cr, Mn, and Co with solar abundances (Scott et al. 2015a). Right panel: similar model in the left panel, except the Sc, Ti, V, Cr, Mn, and Co abundances are artifically increased by a factor of 700. The vertical bar indicates 10 % of the continuum flux.

### 5. The secondary

Binary systems often reveal themselves by the sinusoidal movement of their components' lines in trailed spectra (e.g., Maxted et al. 2000). Figure 8 shows a comparison of a synthetic and an observed "s-curve". To search for lines of the AA Dor secondary, the primary's master spectra (Sect. 4) are subtracted

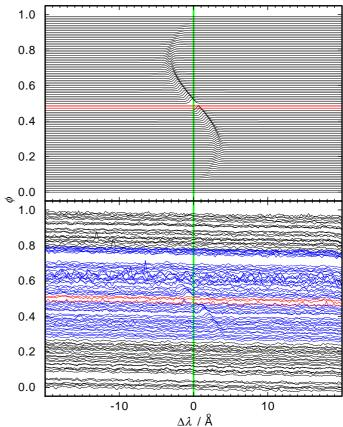


**Fig. 8.** Top: C  $\pi$   $\lambda$  4267.09 Å line in a simulation (with an assumed  $K_{\rm sec} = 230 \, {\rm km/s}$ ).  $\phi$  is the orbital phase. The transit ( $\phi = 0.0$ ) and the occultation ( $\phi = 0.5$ ) of the secondary are simulated. Bottom: the same line in our XSHOOTER observations (bottom). In the online version, the red spectra show the occultation of the secondary. In the blue spectra, C  $\pi$   $\lambda$  4267.09 Å is prominent. The vertical (green) bar indicates the rest wavelength of the line.

from the UVES and XSHOOTER observations with a respective phase-dependent radial-velocity correction.

To make the application of the s-curve method easier, we have created a tool (Sect. 5.1) that even detects weak s-curves and that measures the orbital period and velocity amplitude via this sensitive visual method.

#### 5.1. The new GAVO tool TLISA

In the framework of the Tübingen GAVO project, we developed the Tübingen Line Identification and Spectrum Analyzer (TLISA) tool that evaluates spectra and visualizes them. The first module, SEarch for Faint Objects in Binary Systems (SEFOBS), allows us to correct for orbital phase and velocity amplitude. Its sensitivity, i.e., the detection limit for lines is demonstrated in Fig. 9.

TLISA is a java<sup>11</sup> tool that can be retrieved freely in its desktop version via http://astro.uni-tuebingen.de/~TLISA. Our XSHOOTER UVB spectra are provided there as a test data package.

<sup>11</sup> https://java.com/en

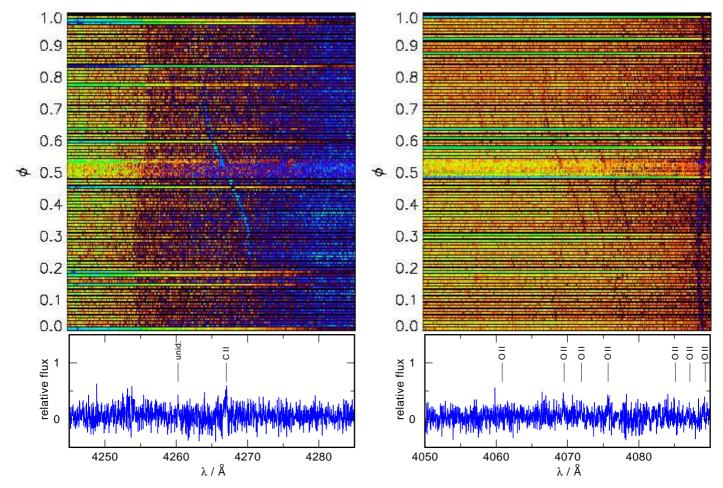


**Fig. 10.** Top: section of the secondary's phase-dependent UVES spectra (4245 Å  $\leq \lambda \leq$  4285 Å). Bottom: single spectrum (2001-01-08T00-53-54.965 UT) in the secondary's rest frame in the respective wavelength interval; "unid." denotes unidentified lines.

5.2. Search for spectral signatures

We applied TLISA to our UVES and XSHOOTER data. Two representative examples for a successful search of a relatively strong and comparatively weak lines in the UVES data are shown in Figs. 10 and 11, respectively. In total, we identified 73 spectral lines that stem from the secondary. For their unambiguous assignment, we calculated TMAP models ( $T_{\rm eff}$  = 20000 K, log g = 5.0), which included H and one metal (C, N, or O) at solar abundance (Asplund et al. 2009), with atomic data from the Tübingen Model-Atom database (TMAD<sup>12</sup>). Although the parameters do not represent the secondary, they are well suited for identification purposes. In particular, we modeled the multiplet line patterns precisely. Table 3 shows the identified lines. We indicate lines that we did not include in our models due to limited model atoms, but are found in the National Institute of Standards and Technology (Kramida et al. 2014) atomic spectra database.

It is worthwhile to note that neither Rauch & Werner (2003) nor Rucinski (2009, and priv. comm.) succeeded in a search for lines of the secondary. Vučković et al. (2008) identified more than 20 narrow emission lines, mainly of C  $\pi$  and O  $\pi$  and broad Balmer emission lines with core absorption (Table 3 indicates those explicitly mentioned by the authors). All these groups had the same UVES data at their disposal.

**Fig. 11.** Same as Fig. 10 for 4050 Å  $\leq \lambda \leq$  4090 Å.

Table 2. Radial-velocity amplitudes for selected lines of the secondary.

$\lambda_{ m lab}$ / Å	$K_{\rm sec}$ / km/s	Instrument
3920.68	228.7	UVES
4069.62	213.5	UVES
4072.15	213.3	UVES
4075.86	220.0	UVES
4089.29	233.0	UVES
4101.74	239.1	UVES
4119.22	217.7	UVES
4185.44	227.6	UVES
4189.79	214.0	UVES
4267.09	223.3	UVES
4414.91	228.5	UVES
4416.97	228.4	UVES
4699.22	214.7	UVES
4705.35	208.4	UVES
4069.62	220.3	XSHOOTER UVB
4101.74	225.4	XSHOOTER UVB
4267.09	229.8	XSHOOTER UVB
4340.47	219.5	XSHOOTER UVB
4414.91	222.1	XSHOOTER UVB
4416.97	215.7	XSHOOTER UVB
4861.33	213.3	XSHOOTER UVB
7065.19	210.2	XSHOOTER VIS

**Notes.** Wavelengths correspond to Table 3.

<sup>12</sup> http://astro.uni-tuebingen.de/~TMAD

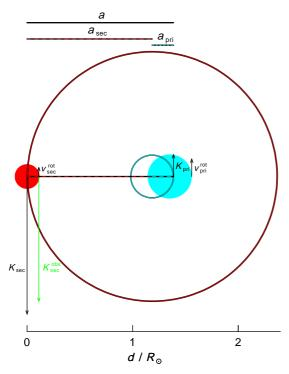


Fig. 12. Dimensions (drawn to scale), orbits, and velocities of AA Dor.

We used TLISA to determine the radial-velocity amplitude of the secondary and arrived at an average of  $K_{\rm sec}^{\rm obs}$  =  $220 \pm 10 \, \rm km/s$ . To control the quality of this graphical method, we used the image reduction and analysis facility (IRAF<sup>13</sup>) to measure the wavelengths shifts for selected lines in all spectra (Table 2). We measured instrument-average values of  $K_{\rm sec}^{\rm obs}$  =  $222.2 \pm 2.5 \, \rm km/s$  and  $K_{\rm sec}^{\rm obs}$  =  $220.9 \pm 2.3 \, \rm km/s$  (1  $\sigma$  errors) from the UVES and XSHOOTER UVB data. In the XSHOOTER VIS data, only one line could be used from which we determined  $K_{\rm sec}^{\rm obs}$  =  $210.2 \pm 6.4 \, \rm km/s$ . Weighted by the number of individual results and the 13 times better spectral resolution of UVES, we calculate an average value of  $K_{\rm sec}^{\rm obs}$  =  $222.1 \pm 3.5 \, \rm km/s$ . This value is almost equal to the TLISA value (above) and demonstrates well that TLISA is a quite powerful tool.

Figure 12 illustrates the dimensions and velocities of AA Dor. All rotations and orbital motions are counterclockwise. The parameter  $K_{\text{sec}}^{\text{obs}}$  is measured.

Our spectra show clearly that a day and a night side exist (Fig. 8). Neither an efficient horizontal energy flow nor a significantly unsynchronized rotation of the secondary<sup>14</sup> yield an isothermal surface structure.

The assumption of a synchronized rotation of the secondary and of a strict separation of an irradiated day side and a nonirradiated night side is a simplification (cf., Barman et al. 2004). In reality, horizontal energy flows (heat conduction or winds) couples the two sides. Improved 1.5 dimensional (1.5 D) modeling of irradiated planets (Barman et al. 2005) have shown that the temperature and mean-intensity distribution at a planet's surface resemble a horseshoe shape (Hauschildt et al. 2008). Better

spectra with much higher S/N and resolution would allow us to investigate this effect and crucially constrain future (3 D) modeling.

However,  $a_{\rm sec}$  calculated from  $K_{\rm sec}^{\rm obs}$  would be too small. Since no detailed model for the surface structure or phase-dependent spectra of the secondary of AA Dor exist, we estimate that the center of gravity of the measured emission lines is dominated by a region that lies toward the irradiating primary star, but not very much off the secondary's orbital path. The maximum error is  $K_{\rm sec}^{\rm corr} = 2\pi R_{\rm sec}/P$  (emission region lies closest to the primary). We assume a quarter of that value with respective error range  $(5.4_{-5.4}^{+16.2}\,{\rm km/s}, {\rm with}\,R_{\rm sec} = 0.1112\,R_{\odot}, {\rm Sect.}\,6)$ . In addition, the secondary is assumed to perform a synchronous rotation with  $v_{\rm sec}^{\rm rot} = 2\pi R_{\rm sec}/P$ . Projected at our assumed main emission region, we use  $v_{\rm sec}^{\rm rot,em} = \sin\alpha\,v_{\rm sec}^{\rm rot}$  (with  $\alpha = 15^{\circ}$ ). Thus, the real orbital velocity of the secondary is

$$K_{\text{sec}} = K_{\text{sec}}^{\text{obs}} + v_{\text{sec}}^{\text{rot,em}} + K_{\text{sec}}^{\text{corr}}$$
.

In the case of AA Dor, we calculate  $K_{\rm sec}=(222.1\pm3.5)+(5.4\pm0.6)+(5.4^{+16.2}_{-5.4})~{\rm km/s}=232.9^{+16.6}_{-6.5}~{\rm km/s}$ . This is, within its error limits, well in agreement with the previously determined value of  $K_{\rm sec}\geq 230\pm 10~{\rm km/s}$  given by Vučković et al. (2008) and the estimate of  $K_{\rm sec}=240\pm20~{\rm km/s}$  by Müller et al. (2010).

### 5.3. Spectrum of the secondary

We successfully extracted the spectrum of the secondary's irradiated side (Fig. 13) from those XSHOOTER UVB spectra where C II  $\lambda$  4267.09 Å (Fig. 8) is prominent. Although we observed spectrophotometric standard stars at the beginning and the end of the night, the observing conditions that were widely varying on short timescales during our XSHOOTER night (see http://astro.uni-tuebingen.de/~rauch/ESO\_092.C-0692.gif for an impression) hampered the flux calibration and, thus, our ability to achieve the predicted, better quality even in the coadded spectrum.

In the XSHOOTER UVB, VIS, and NIR spectra (Fig. 14), we did not find any significant, unambiguous spectral features of a (nonirradiated) low-mass dwarf star (e.g., Li et al. 2014; Littlefair et al. 2014; Manjavacas et al. 2014). In this phase, the expected secondary's contribution to the composite spectrum of AA Dor is of the order of 0.1% in the NIR. Our UVES and XSHOOTER spectra are not good enough to measure this. The small deviations between the individual observations stem most likely from variations of the telluric absorption during the night.

# 5.4. Inspection of the FUSE observations

The PHOENIX<sup>15</sup> (Hauschildt & Baron 2009, 2010; Baron et al. 2010) model-atmosphere calculations for the irradiated secondary by Barman et al. (2004) show that its strongest lines are located in the ultraviolet (Fig. 15), especially in the FUSE wavelength range (910 Å  $\lesssim \lambda \lesssim 1188$ Å).

To calculate the composite spectrum of AA Dor, the synthetic spectra of the primary (Klepp & Rauch 2011) and the secondary (Barman et al. 2004) were scaled with  $R_{\rm pri}^2$  and  $R_{\rm sec}^2$  (Sect. 6), respectively. The contribution of the secondary to the composite spectrum is shown in Fig. 16.

Therefore, we analyzed the 12 individual spectra (planned exposure time of 200 s each) that we obtained with FUSE (Ob-

http://iraf.noao.edu, IRAF is distributed by the National Optical Astronomy Observatory, which is operated by the Associated Universities for Research in Astronomy, Inc., under cooperative agreement with the National Science Foundation.

 $<sup>^{14}</sup>$  The rotation of the primary is not synchronized yet (Müller et al. 2010).

http://www.hs.uni-hamburg.de/EN/For/ThA/phoenix

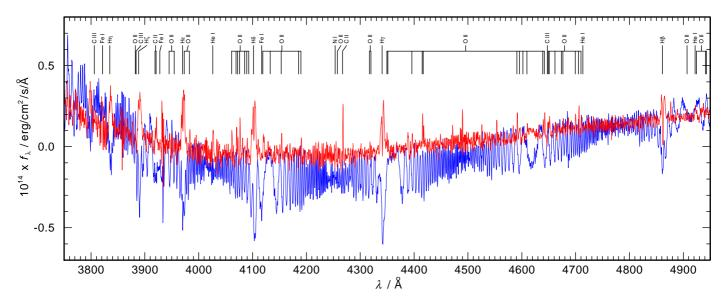


**Fig. 13.** Extracted XSHOOTER UVB spectra of the secondary with the primary master spectrum (Sect. 4) subtracted. The spectra are processed with a Savitzky-Golay low-pass filter (Savitzky & Golay 1964). Red: five spectra coadded just before occultation; blue: five spectra coadded just before transit. The identified lines (Table 3) are marked.

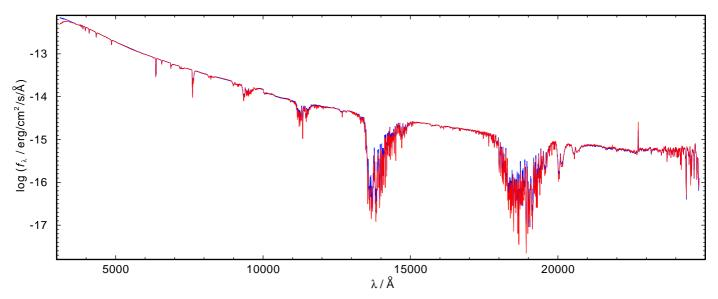


**Fig. 14.** XSHOOTER spectra (smoothed with a Gaussian with a FWHM of 10 Å for clarity) during transit of the secondary (red, ten individual spectra next to  $T_0$  coadded) and during its occultation (blue, three spectra coadded).

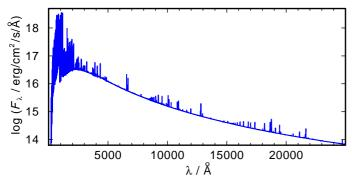


**Fig. 15.** Synthetic spectrum of the irradiated hemisphere of the secondary of AA Dor.

sId D0250101000, 2003-08-29, four observations, total exposure time of 731 s, D0250102000, 2004-06-22, eight observa-

tions,  $1623 \, \text{s}$ ). They cover about an eighth of the orbit of AA Dor (Fig. 17).

The procedure for analyzing the FUSE data was similar to that described above for the UVES and XSHOOTER spectra. First, we measured the velocity offsets from one exposure to the next from the ISM features and coaligned the exposures on these. Then, we measured velocity offsets of the photospheric features (C III, Si IV, and P V) relative to the ISM lines for each exposure and shifted the exposures in velocity space to coalign on the photospheric features. The phase coverage, while not complete, adequately determined the orbital phase for each exposure and confirms the phase predicted from the measured period. The phase-aligned spectra were then combined to produce a template of the primary star. As described above, any features of the secondary star spectrum should be widely dispersed in velocity space and should leave no imprint on this template. This template was shifted to match the velocity of the primary star in each exposure

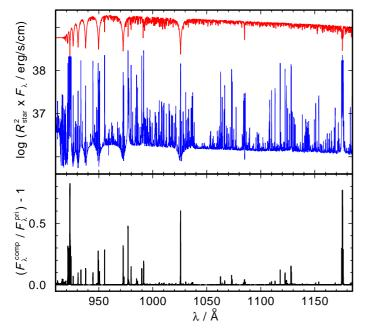


**Fig. 16.** Top panel: contributions of the primary and the secondary to the composite flux of AA Dor in the FUSE wavelength range, convolved with rotational profiles using  $v_{\rm pri}^{\rm rot} = 31.8$  km/s (Rucinski 2009) and  $v_{\rm sec}^{\rm rot} = 21.5$  km/s (calculated from  $R_{\rm sec} = 0.1112$ , Sect. 6). The FUSE resolution was simulated by a subsequent convolution with a Gaussian (FWHM = 0.05 Å). Bottom panel: ratio of the composite flux to the primary's flux.

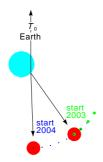


**Fig. 17.** Same as Fig. 1, for our FUSE observations (2003: four big, green dots, 2008: eight small, blue dots).

and then subtracted. We computed the velocity offset for the secondary star relative to the primary, based on our orbital solution (Sect. 3) and orbital velocity (Sect. 5.2). We then shifted each template-subtracted spectrum in velocity space by the predicted velocity offset of the secondary star, and combined the resulting spectra. Unfortunately, no features obviously appear to increase in significance in the coadded FUSE spectrum. Even an individual search for C<sub>II</sub>-III and O<sub>II</sub>-III lines remains entirely negative, although the spectra were taken in both years directly after the secondary's occultation (Fig. 17) where the emission lines are strongest. This nondetection is unexplained. It appears possible that the contribution of the secondary to the composite spectrum of AA Dor in the FUSE wavelength range is overestimated by the current model (Fig. 16). A more thorough exploration of these models is beyond the scope of the present paper and will be the subject of a future study.

#### 6. Orbit dimensions, masses, and radii

With both radial-velocity amplitudes known,  $K_{\rm pri}=40.15\pm0.11\,{\rm km/s}$  (Müller et al. 2010) and  $K_{\rm sec}=232.9^{+16.6}_{-6.5}$ , km/s, we determined the dimensions, masses, and radii of the components of AA Dor. Their orbital radii and the distance of the stars were calculated with

$$a_{\text{pri}} = \frac{P \cdot K_{\text{pri}}}{2\pi} = 0.2074 \pm 0.0006 R_{\odot}$$
 $a_{\text{sec}} = \frac{P \cdot K_{\text{sec}}}{2\pi} = 1.2029^{+0.0857}_{-0.0336} R_{\odot}$ 
 $a = a_{\text{pri}} + a_{\text{sec}} = 1.4102^{+0.0863}_{-0.0341} R_{\odot}$ .

The total mass of the system is

$$M = \frac{4\pi^2 a^3}{G \cdot P^2} = 0.5516^{+0.1076}_{-0.0341} \, M_{\odot}$$

(with the gravitational constant G). With  $K_{pri}M_{pri} = K_{sec}M_{sec}$ , the components' masses are

$$\begin{array}{ll} M_{\rm pri} & = 0.4705^{+0.0975}_{-0.0354}\,M_\odot \\ M_{\rm sec} & = 0.0811^{+0.0184}_{-0.0102}\,M_\odot \end{array}.$$

The radius of the primary is

$$R_{\rm pri} = \sqrt{M_{\rm pri} \cdot G/g_{\rm pri}} = 0.2113^{+0.0346}_{-0.0195} R_{\odot} ,$$

where  $g_{\rm pri}$  is its surface gravity. Kilkenny et al. (1979) determined  $R_{\rm pri}/R_{\rm sec}=1.9$ . Therefore the secondary's radius is  $R_{\rm sec}=0.1112^{+0.0182}_{-0.0102}\,R_{\odot}$ .

#### 7. Results and conclusions

The extracted secondary's spectrum allows us to investigate its nature. A cool brown dwarf shows, for  $T_{\rm eff} \lesssim 1200\,\rm K$ , a typical spectrum that is dominated by NH<sub>3</sub> and CH<sub>4</sub> bands (see, for example, Burningham et al. 2008). In contrast, a late M-type dwarf exhibits, e.g., TiO bands (Kirkpatrick et al. 1993). We did not succeed in extracting the spectrum of the cool side of the secondary. However, both types exhibit emission lines of C II and O II (as already identified by Vučković et al. 2008) only due to irradiation of the primary and thus, the heating of one hemisphere.

We have identified 73 lines of the secondary (Table 3), i.e., the number of identified lines was increased by about a factor of three. This was possible because of the consequent implementation of the s-curve method in the VO tool TLISA, which allows us to search even for very weak lines. The identified lines stem mainly from C  $\pi$  -  $\pi$  and O  $\pi$ .

To make progress on the understanding of the nature of the secondary and, hence, the whole system AA Dor, further UVES observations in its red arm  $(4200 \, \text{Å} \ge \lambda \ge 11000 \, \text{Å})$  on a dark night with superb seeing conditions are highly desirable.

We improved the period measurement of Rauch & Werner (2003) because of the extended time interval and verified the period of  $P=22597.03320768\pm0.0000691$  s, which was determined from the light curve of AA Dor by Kilkenny (2011). We measured an orbital velocity of  $K_{\rm sec}=232.9^{+16.6}_{-6.5}\,{\rm km/s}$  for the secondary. We determined masses of  $M_{\rm pri}=0.4705^{+0.0975}_{-0.0354}\,M_{\odot}$  for the primary star and of  $M_{\rm sec}=0.0811^{+0.0162}_{-0.0102}\,M_{\odot}$  for

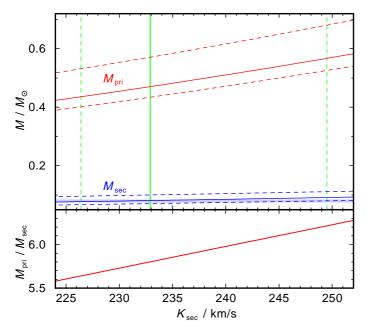


**Fig. 18.** Top: dependency of the components' masses (red: primary dashed lines show the error range, blue: secondary) on the orbital velocity of the secondary (for  $K_{\rm pri}=40.15\,{\rm km/s}$ , Müller et al. 2010). The light blue horizontal region indicates the hydrogen-burning mass limit (Chabrier & Baraffe 1997). The green thick line shows our determination of  $K_{\rm sec}=232.9\,{\rm km/s}$ . The error range is indicated by the green dashed lines.

the secondary star. The secondary's mass is fully overlapping (Fig. 18) with the hydrogen-burning mass limit (0.075 – 0.085  $M_{\odot}$ , Chabrier & Baraffe 1997) and, thus, it is still not possible to decide about the nature of the object.

Our primary and secondary masses agree perfectly with those of Klepp & Rauch (2011,  $M_{\rm pri}=0.4714\pm0.0050\,M_{\odot}$ ,  $M_{\rm sec}=0.0788^{+0.0075}_{-0.0063}\,M_{\odot}$ ). They assumed a solar He abundance (Y=0.288) on the horizontal branch (HB) and determined  $M_{\rm pri}$  by a comparison with respective post-EHB evolutionary tracks (Fig. 19) of Dorman et al. (1993). Since AA Dor had experienced a common-envelope event and its present abundance pattern (Table 1) exhibits the interplay of gravitational settling and radiative levitation (cf. Rauch 2000), any information about its former photospheric abundances is lost. However, the assumption of solar abundances for AA Dor on the HB appears reasonable.

Our masses also agree well with those of Hilditch et al. (2003,  $0.33\,M_\odot \le M_{\rm pri} \le 0.47\,M_\odot$  and  $0.064\,M_\odot \le M_{\rm sec} \le 0.082\,M_\odot$ ). The values of Müller et al. (2010,  $M_{\rm pri} = 0.510^{+0.125}_{-0.108}\,M_\odot$ ,  $M_{\rm sec} = 0.085^{+0.031}_{-0.023}\,M_\odot$ ) agree with ours within error limits.

Detailed 3D modeling of the phase-dependent spectrum of the irradiated secondary of AA Dor that considers horizontal energy flows is highly desirable to verify our assumptions for the correction of the observed  $K_{\rm sec}^{\rm obs}$  in Sect. 5.2. Our primary mass  $M_{\rm pri}=0.47\,M_{\odot}$ , which was calculated with  $K_{\rm sec}=232.9$ , km/s, agrees with the mass interval of  $0.33\,M_{\odot} \leq M_{\rm pri} \leq 0.47\,M_{\odot}$  (Hilditch et al. 2003, from light-curve analysis). Higher values of  $K_{\rm sec}$  yield higher values of  $M_{\rm pri}$  (Fig. 18). E.g.,  $K_{\rm sec}=240$ , km/s results in  $M_{\rm pri}=0.5104^{+0.1061}_{-0.0424}\,M_{\odot}$  which is, even within error limits, outside the mass interval (see above).

Acknowledgements. DH and TR are supported by the German Aerospace Center (DLR, grants 50 OR 1501 and 05 OR 1402, respectively). The GAVO project at Tübingen was supported by the Federal Ministry of Education

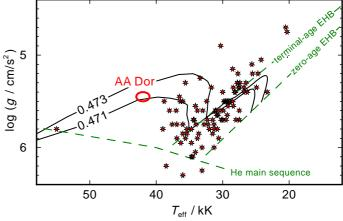


**Fig. 19.** Location of the primary of AA Dor in the  $T_{\rm eff} - \log g$  plane (the ellipse indicates the error limits given by Klepp & Rauch 2011) compared to sdBs and sdOBs from Edelmann (2003). Post-EHB tracks from Dorman et al. (1993, full black lines, labeled with the respective stellar masses in  $M_{\odot}$ , solar H/He ratio and solar metallicity on the HB) are also shown for comparison.

and Research (BMBF, grants 05 AC 6 VTB, 05 AC 11 VTB). The TLISA tool (http://astro.uni-tuebingen.de/~TLISA) used for this paper was constructed as part of the activities of the German Astrophysical Virtual Observatory. The UVES and XSHOOTER spectra used in this analysis were obtained as parts of ESO Service Mode runs, programs 066.D-1800 and 092.C-0692, respectively. We thank David Kilkenny for his help in determining the exact time of the secondary's occultation during our XSHOOTER observations, Roger Wesson who had performed these observations and successfully covered this critical time, and Travis Barman who put the irradiated spectrum of the secondary at our disposal. Some of the data presented in this paper were obtained from the Mikulski Archive for Space Telescopes (MAST). STScI is operated by the Association of Universities for Research in Astronomy, Inc., under NASA contract NAS5-26555. Support for MAST for non-HST data is provided by the NASA Office of Space Science via grant NNX09AF08G and by other grants and contracts. This research has made use of NASA's Astrophysics Data System and the SIMBAD database, operated at CDS, Strasbourg, France.

#### References

Almeida, L. A., Jablonski, F., Tello, J., & Rodrigues, C. V. 2012, MNRAS, 423, 478

Asplund, M., Grevesse, N., Sauval, A. J., & Scott, P. 2009, ARA&A, 47, 481 Barlow, B. N., Kilkenny, D., Drechsel, H., et al. 2013, MNRAS, 430, 22

Barman, T. S., Hauschildt, P. H., & Allard, F. 2004, ApJ, 614, 338 Barman, T. S., Hauschildt, P. H., & Allard, F. 2005, ApJ, 632, 1132

Baron, E., Chen, B., & Hauschildt, P. H. 2010, PHOENIX: A General-purpose State-of-the-art Stellar and Planetary Atmosphere Code, Astrophysics Source

Code Library
Bergeron, P., Wesemael, F., Lamontagne, R., & Chayer, P. 1993, ApJ, 407, L85
Burningham, B., Pinfield, D. J., Leggett, S. K., et al. 2008, MNRAS, 391, 320
Chabrier, G. & Baraffe, I. 1997, A&A, 327, 1039

Chabrier, G., Baraffe, I., Allard, F., & Hauschildt, P. 2000, ApJ, 542, 464 Dorman, B., Rood, R. T., & O'Connell, R. W. 1993, ApJ, 419, 596

Edelmann, H. 2003, Dissertation, University of Erlangen-Nuremberg Fitzpatrick, E. L. 1999, PASP, 111, 63

Fleig, J., Rauch, T., Werner, K., & Kruk, J. W. 2008, A&A, 492, 565

Geckeler, R. D., Schuh, S., Dreizler, S., et al. 2014, TRIPP: Time Resolved Imaging Photometry Package, Astrophysics Source Code Library
 Geier, S., Heber, U., Podsiadlowski, P., et al. 2010, A&A, 519, A25

Hauschildt, P. H., Barman, T., & Baron, E. 2008, Physica Scripta Volume T, 130, 014033

Hauschildt, P. H. & Baron, E. 2009, A&A, 498, 981

Hauschildt, P. H. & Baron, E. 2010, A&A, 509, A36

Heber, U. 2009, ARA&A, 47, 211

Hilditch, R. W., Harries, T. J., & Hill, G. 1996, MNRAS, 279, 1380Hilditch, R. W., Kilkenny, D., Lynas-Gray, A. E., & Hill, G. 2003, MNRAS, 344, 644

Kilkenny, D. 2011, MNRAS, 412, 487

Kilkenny, D., Hilditch, R. W., & Penfold, J. E. 1978, MNRAS, 183, 523

Kilkenny, D., Hilditch, R. W., & Penfold, J. E. 1979, MNRAS, 187, 1

Kirkpatrick, J. D., Kelly, D. M., Rieke, G. H., et al. 1993, ApJ, 402, 643

Klepp, S. & Rauch, T. 2011, A&A, 531, L7

Kramida, A., Yu. Ralchenko, Reader, J., & and NIST ASD Team. 2014, NIST Atomic Spectra Database (ver. 5.2), [Online]. Available: http://physics.nist.gov/asd [April 13, 2018]. National Institute of Standards and Technology, Gaithersburg, MD.

Li, L., Zhang, F., Han, Q., Kong, X., & Gong, X. 2014, MNRAS, 445, 1331

Littlefair, S. P., Casewell, S. L., Parsons, S. G., et al. 2014, MNRAS, 445, 2106

Livio, M. & Soker, N. 1984, MNRAS, 208, 783

Manjavacas, E., Bonnefoy, M., Schlieder, J. E., et al. 2014, A&A, 564, A55

Maxted, P. F. L., North, R. C., & Marsh, T. R. 2000, The Newsletter of the Isaac Newton Group of Telescopes, 3, 7

Müller, S., Geier, S., & Heber, U. 2010, Ap&SS, 329, 101

Napiwotzki, R. & Rauch, T. 1994, A&A, 285, 603

Rauch, T. 2000, A&A, 356, 665

Rauch, T. 2004, Ap&SS, 291, 275

Rauch, T. 2012, in Astronomical Society of the Pacific Conference Series, Vol. 452, Fifth Meeting on Hot Subdwarf Stars and Related Objects, ed. D. Kilkenny, C. S. Jeffery, & C. Koen, 111

Rauch, T. & Deetjen, J. L. 2003, in Astronomical Society of the Pacific Conference Series, Vol. 288, Stellar Atmosphere Modeling, ed. I. Hubeny, D. Mihalas, & K. Werner, 103

Rauch, T. & Werner, K. 2003, A&A, 400, 271

Rauch, T., Werner, K., Biémont, É., Quinet, P., & Kruk, J. W. 2012, A&A, 546, A55

Rauch, T., Werner, K., Quinet, P., & Kruk, J. W. 2014a, A&A, 564, A41

Rauch, T., Werner, K., Quinet, P., & Kruk, J. W. 2014b, A&A, 566, A10

Rauch, T., Werner, K., Quinet, P., & Kruk, J. W. 2015, A&A, 577, A6

Ritter, H. 1986, A&A, 169, 139

Ritter, H. & Kolb, U. 2003, A&A, 404, 301

Rucinski, S. M. 2009, MNRAS, 395, 2299

Savitzky, A. & Golay, M. J. E. 1964, Analytical Chemistry, 36, 1627

Schaffenroth, V., Barlow, B. N., Drechsel, H., & Dunlap, B. H. 2015, ArXiv 1502.04459

Schaffenroth, V., Geier, S., Drechsel, H., et al. 2013, A&A, 553, A18

Schaffenroth, V., Geier, S., Heber, U., et al. 2014, A&A, 564, A98

Schreiber, M. R. & Gänsicke, B. T. 2003, A&A, 406, 305

Schuh, S. L., Dreizler, S., Deetjen, J. L., & Göhler, E. 2003, Baltic Astronomy, 12, 167

Scott, P., Asplund, M., Grevesse, N., Bergemann, M., & Sauval, A. J. 2015a, A&A, 573, A26

Scott, P., Grevesse, N., Asplund, M., et al. 2015b, A&A, 573, A25

Tremblay, P.-E. & Bergeron, P. 2009, ApJ, 696, 1755

Vernet, J., Dekker, H., D'Odorico, S., et al. 2011, A&A, 536, A105

Vučković, M., Østensen, R., Bloemen, S., Decoster, I., & Aerts, C. 2008, in Astronomical Society of the Pacific Conference Series, Vol. 392, Hot Subdwarf Stars and Related Objects, ed. U. Heber, C. S. Jeffery, & R. Napiwotzki, 199 Werner, K. 1996, ApJ, 457, L39

Werner, K., Deetjen, J. L., Dreizler, S., et al. 2003, in Astronomical Society of the Pacific Conference Series, Vol. 288, Stellar Atmosphere Modeling, ed. I. Hubeny, D. Mihalas, & K. Werner, 31

Werner, K., Dreizler, S., & Rauch, T. 2012a, TMAP: Tübingen NLTE Model-Atmosphere Package, Astrophysics Source Code Library

Werner, K., Rauch, T., Ringat, E., & Kruk, J. W. 2012b, ApJ, 753, L7

**Table 3.** Identified lines of the secondary in AA Dor. The subscripts obs and lab denote observed (at  $\phi=0.5$ ) and laboratory-measured wavelengths, respectively. In case lines are found in both spectra,  $\lambda_{\rm obs}$  is measured in the UVES spectrum. Columns 4 and 5 indicate in which spectrum they are identified.

$\lambda_{ m obs}/$ Å	$\lambda_{\mathrm{lab}}/$ Å	Ion	UVES	XSHOOTER
3805.79	3806.12	Сшс	×	UVB
3820.61	3821.18	Fe i <sup>b,c</sup>	×	UVB
3835.01	3835.39	$H\eta$	×	UVB
3881.96	3882.19	O II <sup>c</sup>	×	
3883.83	3883.82	$C III^c$	×	
3888.21	3889.02	$H\zeta$	×	UVB
3918.83	3918.97	Сп	×	UVB
3920.67	3920.68	Сп	×	UVB
3927.27	3927.74	Fe i <sup>b,c</sup>		UVB
3944.80	3945.04	Оп	×	
3954.14	3954.36	Оп	×	UVB
3969.95	3970.08	$H\epsilon$	×	UVB
3973.07	3973.26	Оп	×	
4026.32	4026.21	Не і	×	UVB
4060.84	4061.03	$O II_p$	×	
4069.45	4069.62	Оп	×	UVB
4072.07	4072.15	Оп	×	UVB
4075.77	4075.86	Оп	×	UVB
4085.05	4085.11	Оп	×	UVB
4087.15	4087.15	Оп	×	UVB
4089.05	4089.29	Оп <sup>b,c</sup>	×	UVB
4092.75	4092.93	Оп	×	OVD
4101.69	4101.74	$H \delta^a$	×	UVB
4116.64	4116.95	Fe i <sup>b,c</sup>		OVD
4119.02	4110.93	Оп	×	
4119.02	4119.22	Оп		
		Оп <sup>b</sup>	×	
4185.30	4185.44		×	
4189.76	4189.79	Опр	×	III/D
4253.60	4253.39	Nı	×	UVB
4257.34	4257.54	Оп	×	UVB
4267.40	4267.09	Спа	×	UVB
4317.02	4317.14	OII	×	UVB
4319.79	4319.87	O 11 <sub>p</sub>	×	UVB
4340.56	4340.47	Нγ	×	UVB
4349.41	4349.43	O 11 <sup>a</sup>	×	
4351.25	4351.26	Оп	×	
4395.75	4395.93	Оп		UVB
4415.02	4414.91	O 11 <sup>a</sup>	×	UVB
4416.95	4416.97	O 11 <sup>a</sup>	×	UVB
4590.81	4590.97	OII	×	UVB
4595.96	4595.96	OII	×	UVB
4602.43	4602.13	Оп		UVB
4609.66	4609.44	$O II^{b,c}$	×	UVB
4638.74	4638.86	OII	×	UVB
4641.81	4641.81	OII	×	UVB
4647.28	4647.72	$C III^{b,c}$	×	UVB
4649.05	4649.13	Оп	×	UVB
4650.59	4650.84	Оп	×	UVB
4661.67	4661.63	OII	×	
4673.93	4673.73	$O II_c$	×	
4676.08	4676.24	OII	×	
4699.01	4699.22	OII	×	
4705.16	4705.35	OII	×	
4710.09	4710.01	$O \Pi_p$	×	
4713.64	4713.38	Не і	×	
4861.38	4861.33	$H\beta$	×	UVB

Table 3. continued.

λ <sub>obs</sub> / Å	λ <sub>lab</sub> / Å	Ion	UVES	XSHOOTER
4906.86	4906.83	Опр		UVB
4921.97	4921.93	Не і	×	UVB
4924.52	4924.53	$O_{II}^{b,c}$	×	UVB
4940.97	4941.07	Оп	×	UVB
4942.82	4943.01	OII	×	UVB
5875.63	5875.62	Не і		VIS
6151.31	6151.62	Fe i <sup>b,c</sup>		VIS
6562.82	6562.79	$H\alpha$		VIS
6578.06	6578.05	Сп		VIS
6582.90	6582.88	Сп		VIS
6780.09	6780.50	Сп		VIS
6783.83	6783.91	Сп		VIS
6787.38	6787.21	Сп		VIS
7065.32	7065.19	Не і		VIS
8558.13	8558.52	Fe i <sup>b,c</sup>		VIS
9903.74	9904.06	Fе п <sup>b,c</sup>		VIS
17654.46	17654.53	Оп		NIR

**Notes.** (a) identified and mentioned by Vučković et al. (2008), (b) NIST wavelength, line not included in our models, (c) uncertain

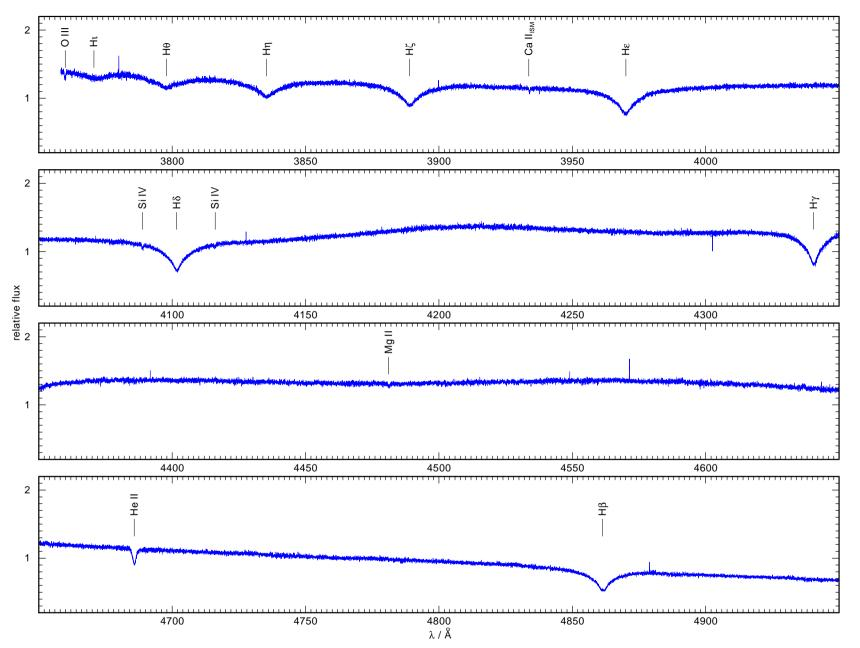


**Fig. 2.** UVES spectrum (blue, start time 2001-01-08T00-27-37.434 UT). Identified lines of the primary are marked. ISM denotes interstellar lines.

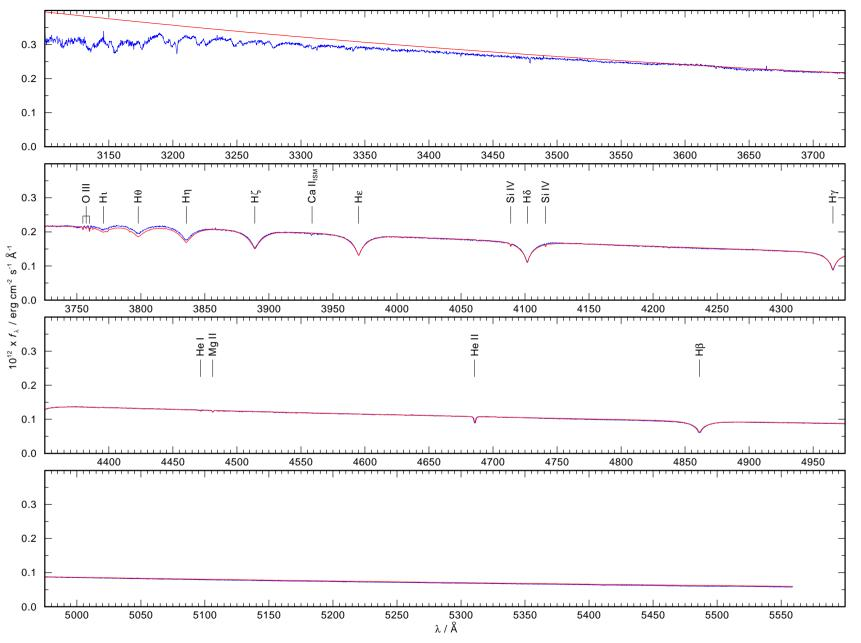


**Fig. 3.** XSHOOTER spectrum (blue, start time 2014-01-08T02-03-37.877 UT) taken in the UVB arm compared with our final model of the primary (red). Identified lines of the primary are marked. ISM denotes interstellar lines.

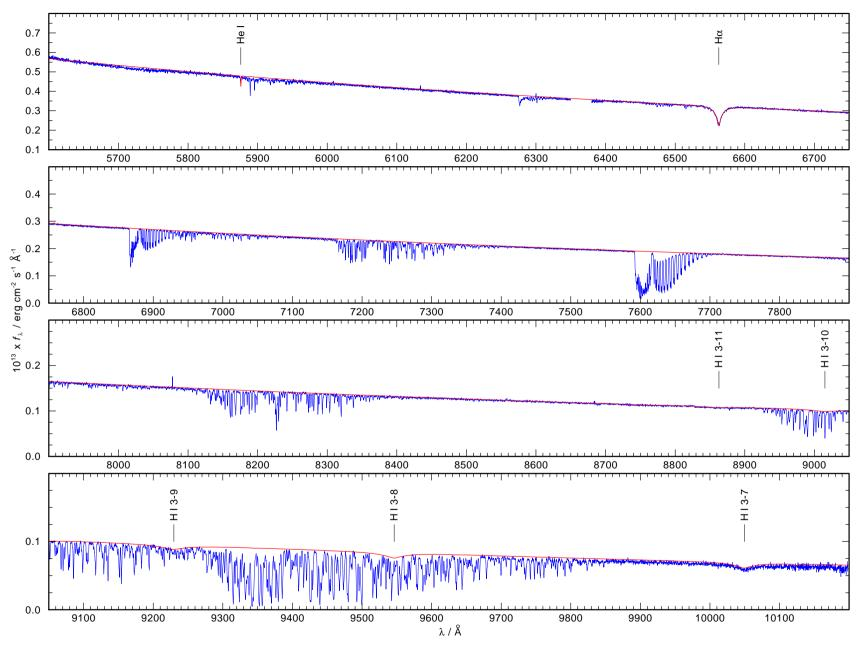


**Fig. 4.** XSHOOTER spectrum (blue, start time 2014-01-08T02-03-43.068 UT) taken in the VIS arm compared with our final model of the primary (red). Identified lines of the primary are marked.

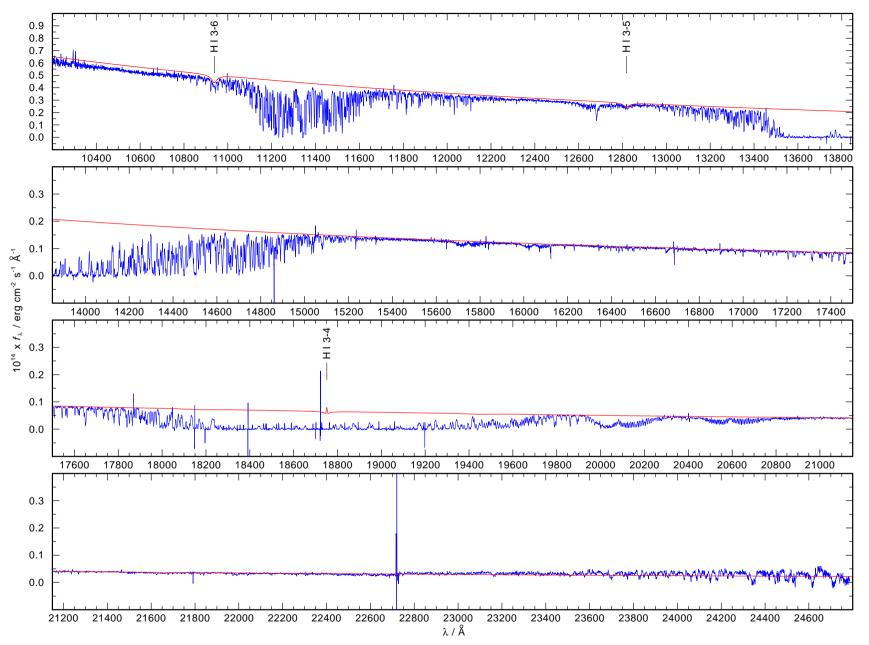


**Fig. 5.** XSHOOTER spectrum (blue, start time 2014-01-08T02-03-45.7348) UT) taken in the NIR arm compared with our final model of the primary (red). Identified lines of the primary are marked.

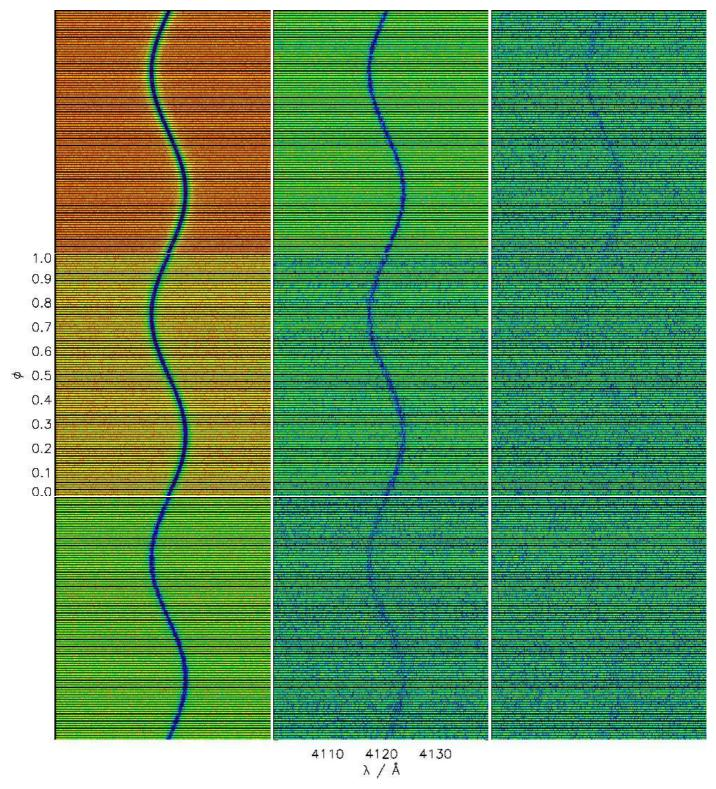


**Fig. 9.** Detection limit for s-curves. A synthetic line profile (phase-dependently shifted with  $K_{\text{sec}} = 230 \,\text{km/s}$ ) at three strengths (equivalent widths of  $W_{\lambda} = 122, 15, \text{ and } 3 \,\text{mÅ}$ , from left to right) is shown for S/N = 50, 25 (approximately our UVES data value), and 10 (top to bottom). All panels show the same wavelength and phase intervals.